

Enhanced structural color generation in aluminum metamaterials coated with a thin polymer layer

Fei Cheng,¹ Xiaodong Yang,^{1,3} Daniel Rosenmann,² Liliana Stan,² David Czaplewski,² and Jie Gao^{1,4}

¹Department of Mechanical and Aerospace Engineering, Missouri University of Science and Technology, Rolla, MO 65409, USA

²Center for Nanoscale Materials, Argonne National Laboratory, Argonne, IL 60439, USA

³yangxia@mst.edu

⁴gaojie@mst.edu

Abstract: A high-resolution and angle-insensitive structural color generation platform is demonstrated based on triple-layer aluminum-silica-aluminum metamaterials supporting surface plasmon resonances tunable across the entire visible spectrum. The color performances of the fabricated aluminum metamaterials can be strongly enhanced by coating a thin transparent polymer layer on top. The results show that the presence of the polymer layer induces a better impedance matching for the plasmonic resonances to the free space so that strong light absorption can be obtained, leading to the generation of pure colors in cyan, magenta, yellow and black (CMYK) with high color saturation.

©2015 Optical Society of America

OCIS codes: (050.6624) Subwavelength structures; (240.6680) Surface plasmons; (160.3918) Metamaterials; (330.1690) Color.

References and links

1. T. W. Ebbesen, H. J. Lezec, H. F. Ghaemi, T. Thio, and P. A. Wolff, "Extraordinary optical transmission through sub-wavelength hole arrays," *Nature* **391**(6668), 667–669 (1998).
2. W. L. Barnes, A. Dereux, and T. W. Ebbesen, "Surface plasmon subwavelength optics," *Nature* **424**(6950), 824–830 (2003).
3. E. Ozbay, "Plasmonics: Merging Photonics and Electronics at Nanoscale Dimensions," *Science* **311**(5758), 189–193 (2006).
4. C. Genet and T. W. Ebbesen, "Light in tiny holes," *Nature* **445**(7123), 39–46 (2007).
5. J. A. Schuller, E. S. Barnard, W. Cai, Y. C. Jun, J. S. White, and M. L. Brongersma, "Plasmonics for extreme light concentration and manipulation," *Nat. Mater.* **9**(3), 193–204 (2010).
6. N. Fang, H. Lee, C. Sun, and X. Zhang, "Sub-diffraction-limited optical imaging with a silver superlens," *Science* **308**(5721), 534–537 (2005).
7. D. Inoue, A. Miura, T. Nomura, H. Fujikawa, K. Sato, N. Ikeda, D. Tsuya, Y. Sugimoto, and Y. Koide, "Polarization independent visible color filter comprising an aluminum film with surface-plasmon enhanced transmission through a subwavelength array of holes," *Appl. Phys. Lett.* **98**(9), 093113 (2011).
8. N. Liu, T. Weiss, M. Mesch, L. Langguth, U. Eigenthaler, M. Hirscher, C. Sönnichsen, and H. Giessen, "Planar metamaterial analogue of electromagnetically induced transparency for plasmonic sensing," *Nano Lett.* **10**(4), 1103–1107 (2010).
9. R. Adato, A. A. Yanik, J. J. Amsden, D. L. Kaplan, F. G. Omenetto, M. K. Hong, S. Erramilli, and H. Altug, "Ultra-sensitive vibrational spectroscopy of protein monolayers with plasmonic nanoantenna arrays," *Proc. Natl. Acad. Sci. U.S.A.* **106**(46), 19227–19232 (2009).
10. H. Wei, Z. Wang, X. Tian, M. Käll, and H. Xu, "Cascaded logic gates in nanophotonic plasmon networks," *Nat. Commun.* **2**, 387 (2011).
11. N. C. Lindquist, W. A. Luhman, S.-H. Oh, and R. J. Holmes, "Plasmonic nanocavity arrays for enhanced efficiency in organic photovoltaic cells," *Appl. Phys. Lett.* **93**(12), 123308 (2008).
12. H. A. Atwater and A. Polman, "Plasmonics for improved photovoltaic devices," *Nat. Mater.* **9**(3), 205–213 (2010).
13. A. S. Roberts, A. Pors, O. Albrektsen, and S. I. Bozhevolnyi, "Subwavelength plasmonic color printing protected for ambient use," *Nano Lett.* **14**(2), 783–787 (2014).

14. S. J. Tan, L. Zhang, D. Zhu, X. M. Goh, Y. M. Wang, K. Kumar, C.-W. Qiu, and J. K. W. Yang, "Plasmonic color palettes for photorealistic printing with aluminum nanostructures," *Nano Lett.* **14**(7), 4023–4029 (2014).
15. J. S. Clausen, E. Højlund-Nielsen, A. B. Christiansen, S. Yazdi, M. Grajower, H. Taha, U. Levy, A. Kristensen, and N. A. Mortensen, "Plasmonic metasurfaces for coloration of plastic consumer products," *Nano Lett.* **14**(8), 4499–4504 (2014).
16. T. Xu, Y.-K. Wu, X. Luo, and L. J. Guo, "Plasmonic nanoresonators for high-resolution colour filtering and spectral imaging," *Nat. Commun.* **1**(5), 59 (2010).
17. K. Kumar, H. Duan, R. S. Hegde, S. C. W. Koh, J. N. Wei, and J. K. W. Yang, "Printing colour at the optical diffraction limit," *Nat. Nanotechnol.* **7**(9), 557–561 (2012).
18. Y.-K. R. Wu, A. E. Hollowell, C. Zhang, and L. J. Guo, "Angle-insensitive structural colours based on metallic nanocavities and coloured pixels beyond the diffraction limit," *Sci. Rep.* **3**, 1194 (2013).
19. T. Xu, H. Shi, Y.-K. Wu, A. F. Kaplan, J. G. Ok, and L. J. Guo, "Structural colors: from plasmonic to carbon nanostructures," *Small* **7**(22), 3128–3136 (2011).
20. B. Zeng, Y. Gao, and F. J. Bartoli, "Ultrathin nanostructured metals for highly transmissive plasmonic subtractive color filters," *Sci. Rep.* **3**, 2840 (2013).
21. G. Si, Y. Zhao, J. Lv, M. Lu, F. Wang, H. Liu, N. Xiang, T. J. Huang, A. J. Danner, J. Teng, and Y. J. Liu, "Reflective plasmonic color filters based on lithographically patterned silver nanorod arrays," *Nanoscale* **5**(14), 6243–6248 (2013).
22. F. Cheng, J. Gao, T. S. Luk, and X. Yang, "Structural color printing based on plasmonic metasurfaces of perfect light absorption," *Sci. Rep.* **5**, 11045 (2015).
23. J. Zhang, J.-Y. Ou, N. Papasimakis, Y. Chen, K. F. Macdonald, and N. I. Zheludev, "Continuous metal plasmonic frequency selective surfaces," *Opt. Express* **19**(23), 23279–23285 (2011).
24. V. R. Shrestha, S.-S. Lee, E.-S. Kim, and D.-Y. Choi, "Aluminum plasmonics based highly transmissive polarization-independent subtractive color filters exploiting a nanopatch array," *Nano Lett.* **14**(11), 6672–6678 (2014).
25. G. V. Naik, V. M. Shalaev, and A. Boltasseva, "Alternative plasmonic materials: beyond gold and silver," *Adv. Mater.* **25**(24), 3264–3294 (2013).
26. B. Y. Zheng, Y. Wang, P. Nordlander, and N. J. Halas, "Color-selective and CMOS-compatible photodetection based on aluminum plasmonics," *Adv. Mater.* **26**(36), 6318–6323 (2014).
27. P. R. West, S. Ishii, G. V. Naik, N. K. Emani, V. M. Shalaev, and A. Boltasseva, "Searching for better plasmonic materials," *Laser Photonics Rev.* **4**(6), 795–808 (2010).
28. J. Olson, A. Manjavacas, L. Liu, W.-S. Chang, B. Foerster, N. S. King, M. W. Knight, P. Nordlander, N. J. Halas, and S. Link, "Vivid, full-color aluminum plasmonic pixels," *Proc. Natl. Acad. Sci. U.S.A.* **111**(40), 14348–14353 (2014).
29. F. Cheng, J. Gao, L. Stan, D. Rosenmann, D. Czaplowski, and X. Yang, "Aluminum plasmonic metamaterials for structural color printing," *Opt. Express* **23**(11), 14552–14560 (2015).
30. V. Kulkarni, E. Prodan, and P. Nordlander, "Quantum plasmonics: optical properties of a nanomatryushka," *Nano Lett.* **13**(12), 5873–5879 (2013).
31. Q. Chen and D. R. S. Cumming, "High transmission and low color cross-talk plasmonic color filters using triangular-lattice hole arrays in aluminum films," *Opt. Express* **18**(13), 14056–14062 (2010).
32. Z. Fang, Y.-R. Zhen, L. Fan, X. Zhu, and P. Nordlander, "Tunable wide-angle plasmonic perfect absorber at visible frequencies," *Phys. Rev. B* **85**(24), 245401 (2012).
33. W. Cai, U. K. Chettiar, H.-K. Yuan, V. C. de Silva, A. V. Kildishev, V. P. Drachev, and V. M. Shalaev, "Metamagnetics with rainbow colors," *Opt. Express* **15**(6), 3333–3341 (2007).
34. N. Liu, M. Mesch, T. Weiss, M. Hentschel, and H. Giessen, "Infrared perfect absorber and its application as plasmonic sensor," *Nano Lett.* **10**(7), 2342–2348 (2010).
35. F. Cheng, X. Yang, and J. Gao, "Enhancing intensity and refractive index sensing capability with infrared plasmonic perfect absorbers," *Opt. Lett.* **39**(11), 3185–3188 (2014).
36. M. N. Polyanskiy, Refractive index database. Available at <http://refractiveindex.info> (accessed Feb. 29 2015).
37. C. Wu, B. Neuner, G. Shvets, J. John, A. Milder, B. Zollars, and S. Savoy, "Large-area wide-angle spectrally selective plasmonic absorber," *Phys. Rev. B* **84**(7), 075102 (2011).
38. H.-S. Lee, Y.-T. Yoon, S. S. Lee, S.-H. Kim, and K.-D. Lee, "Color filter based on a subwavelength patterned metal grating," *Opt. Express* **15**(23), 15457–15463 (2007).
39. K. Aydin, V. E. Ferry, R. M. Briggs, and H. A. Atwater, "Broadband polarization-independent resonant light absorption using ultrathin plasmonic super absorbers," *Nat. Commun.* **2**, 517 (2011).
40. M. G. Nielsen, A. Pors, O. Albrechtsen, and S. I. Bozhevolnyi, "Efficient absorption of visible radiation by gap plasmon resonators," *Opt. Express* **20**(12), 13311–13319 (2012).
41. S. He, F. Ding, L. Mo, and F. Bao, "Light absorber with an ultra-broad flat band based on multi-sized slow-wave hyperbolic metamaterial thin-films," *Prog. Electromagnetics Res.* **147**, 69–79 (2014).

1. Introduction

Recently, plasmonic metamaterials and metasurfaces [1–4] have generated great interest due to their ability to strongly confine surface plasmons [5] and control the properties of light at will in various applications, such as optical imaging [6,7] biochemical sensing [8,9]

information processing [5,10] and solar energy harvesting [11,12]. Among all these efforts, structural color printing based on plasmonic metamaterials has recently been demonstrated [13–15], showing not only two-orders of magnitude higher spatial resolution [16–18] compared to the traditional pigment-based color printing techniques, but also a high sustainability [14] and great potential for electro-optic tunability [19]. The majority of previous works on plasmonic color printing are based on nanostructures made of noble metals such as silver [17,18,20–22] and gold [13] due to their lower ohmic losses in the visible spectrum. However, the interband transition of gold limits rendering colors at wavelengths shorter than 550 nm [13,23,24], while silver nanostructures are extremely susceptible to oxidation and sulphidation which results in the degradation of the perceived colors [14,21,25]. Moreover, silver and gold are not compatible with complementary metal oxide semiconductor (CMOS) fabrication processes, which prevent their practical applications [26]. Meanwhile, plasmonic color generation based on aluminum [14,15] has recently obtained extensive interest due to the high plasma frequency of aluminum in the UV region [27] together with its cost-effectiveness and sustainable merits [24,26]. Furthermore, the low quality factor of aluminum plasmonic nanostructures introduces a lower spectral sensitivity for distinct colors and thus gives a large tolerance to critical-dimension control in the fabrication [14].

Although aluminum is an attractive substitute metal material for plasmonic color printing, the color performance of the previously reported aluminum-based platforms is still limited by the loss-induced linewidth broadening of plasmonic resonances [14,27–29], which will significantly reduce the color purity in addition to color saturation or brightness. Furthermore, although aluminum forms a self-limiting impermeable native oxide layer [30] against oxidation and sulphidation, a mechanical protection layer is always desirable for ambient use in practical color printing applications with high reliability and long durability. Here we introduce and demonstrate an aluminum-based structural color generation platform to improve the color purity and saturation that are not well addressed in the previous works. The platform is based on aluminum plasmonic metamaterials supporting plasmonic resonances with strong and narrow-band light absorption in the visible range. A thin transparent polymer layer is coated on top of the metamaterials to not only protect the surface from scratching and contamination but also greatly enhance the color performances. The existence of the polymer layer leads to a better impedance matching for the plasmonic resonant modes to the free space and thus providing enhanced light absorption for the generation of pure colors in cyan, magenta, yellow and black (CMYK) with high saturation. The plasmonic resonance redshift induced by the polymer layer can be readily compensated by geometrical adjustments in the fabrication. Moreover, the color purity and saturation can be further improved by taking advantage of a higher order plasmonic resonance with narrower spectral line width introduced by the polymer layer.

2. Device design and fabrication

The aluminum-based plasmonic color printing metamaterials are fabricated as follows. First, the metal-dielectric-metal three layer stack consisting of a top 30 nm aluminum (Al) layer, a 45 nm silica (SiO₂) spacer and a bottom 100 nm thick Al mirror is deposited at room temperature on a silicon wafer by a combination of reactive magnetron sputtering and electron-beam evaporation, with a base-pressure of 2×10^{-8} Torr. Samples are transferred between physical vapor deposition systems through a load-lock at a pressure of 2×10^{-7} Torr or better. The designed circular hole arrays arranged in triangular lattices with period P and hole radius r are then patterned on the top Al layer using a focused ion beam system (FEI Helios Nanolab 600 DualBeam). Figure 1(a) illustrates a schematic of the aluminum plasmonic metamaterials consisting of three functional layers. Figure 1(b) shows a cross-section scanning electron micrograph (SEM) image of one fabricated sample with $P = 260$ nm and $r = 90$ nm. The transmittance of the metamaterials is totally eliminated ($T = 0$) by the presence of the bottom thick Al layer due to the small penetration depth of light. Here the

triangular lattices are chosen instead of the square lattices, due to the fact that the hole arrays of triangular lattices have a larger wavelength interval between the first two plasmonic resonances compared to that of square lattices with the same lattice periods [31]. Therefore, the color cross-talk between different plasmonic resonances can be greatly reduced to enhance the color purity. Furthermore, the triangular lattice exhibits an inherently polarization independent property [7].

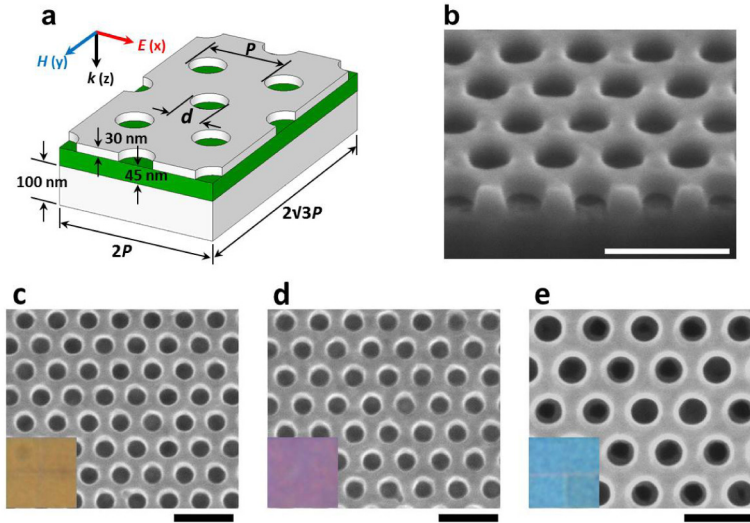


Fig. 1. (a) Schematic of four unit cells of the circular hole arrays of triangular lattice fabricated on the Al-SiO₂-Al triple layer structure. (b) A cross-section SEM image of the fabricated aluminum plasmonic metamaterial with period and hole size of 260 and 180 nm, respectively. (c-e) SEM images of three samples with different geometric parameters of period and hole radius (c: $P = 240$ nm, $r = 75$ nm; d: $P = 270$ nm, $r = 85$ nm; e: $P = 320$ nm, $r = 100$ nm). Insets: Optical reflection microscopy images of the entire $20 \times 20 \mu\text{m}^2$ arrays. Scale bars: 500 nm.

3. Optical response characterization and effect of the presence of a protection layer

The optical response of the fabricated plasmonic metamaterials is characterized in the visible range with an optical reflection measurement setup. Fig. 1(c)-1(e) show the SEM images and bright-field optical microscope images of three selected samples ($20 \times 20 \mu\text{m}^2$) with different periods and hole radii, corresponding to three primary colors of yellow, magenta and cyan in the CMYK color system. Similar to the mechanism of surface plasmon enhanced optical transmission through metallic subwavelength hole arrays [1], highly confined propagating surface plasmons are excited on the top Al layer of the structure. The SiO₂ spacer acts as a bridge to couple surface plasmons on two opposite Al-SiO₂ interfaces [32] within the spacer, forming a magnetic dipole resonance with anti-parallel current flow [33,34]. The coexistence of electric dipole resonance and magnetic dipole resonance of the plasmonic metamaterials results in the matched impedance to the free space, leading to low reflection and thus strong light absorption [35]. As shown in Fig. 2(a), five fabricated plasmonic samples are characterized to investigate the effects of geometrical tunability on the optical reflection spectra and corresponding colors. As the lattice period increases from 240 nm to 370 nm and the hole radius varies from 75 nm to 100 nm, the measured plasmonic resonance wavelength undergoes a redshift from 444 nm to 658 nm and the observed bright-field optical image changes color gradually from dim yellow to bright magenta, cyan and light green. When the lattice period and hole radius increase to 420 nm and 110 nm, respectively, the second-order plasmonic resonance with a narrow line width and near perfect absorption ($A = 1 - R \approx 90\%$) emerges at the wavelength of 443 nm while the first-order resonance is pushed out of the

visible spectrum, leading to a much brighter yellow color appearance as compared to the first sample with 240 nm period and 75 nm hole radius. The fabricated metamaterials are also analyzed with numerical simulations based on the finite element method. The permittivity of Al is obtained from a refractive index database [36] and the simulation results show good agreement with the experimental data.

As mentioned above, a protective layer is always desired for use in harsh ambient environment, in order to keep off not only chemical degradations such as oxidization and contamination but also mechanical damages. In this way, the effects of a protective thin polymer layer on the optical reflection spectra and perceived color performances of the aluminum plasmonic metamaterials are studied. The five fabricated structures are then coated with a 100 nm thick poly(methyl methacrylate) (PMMA) layer. Figure 2(b) shows the measured and simulated optical reflection spectra and respective bright-field microscope images. As compared to the optical reflection curves from the bare structures, the addition of a thin PMMA layer leads to a notable redshift of the resonance wavelength due to the increase of refractive index. Furthermore, the second-order plasmonic resonance is now introduced in the visible range for structures with periods longer than 270 nm. Notably, the reflection intensity at the plasmonic resonance is significantly reduced so that stronger light absorption is achieved for all the metamaterials. For example, for the sample with $P = 270$ nm and $r = 80$ nm, the measured minimum reflection intensity decreases from 0.32 at the resonance of 500 nm for the bare structure to 0.13 at the resonance of 584 nm for the PMMA-coated one. Additionally, near perfect light absorption is obtained ($A \approx 95\%$) for the PMMA-coated metamaterials presenting the second-order plasmonic resonance, as shown in the last two panels of Fig. 2(b). The second-order plasmonic resonance mode also provides a much smaller linewidth (with the full width at half maximum around 55 nm) and larger reflection intensity contrast (about 0.45) for the two PMMA-coated structures with $P = 370$ nm and $P = 420$ nm, enabling the generation of purer and brighter colors with higher saturation compared to the colors obtained from the bare structures.

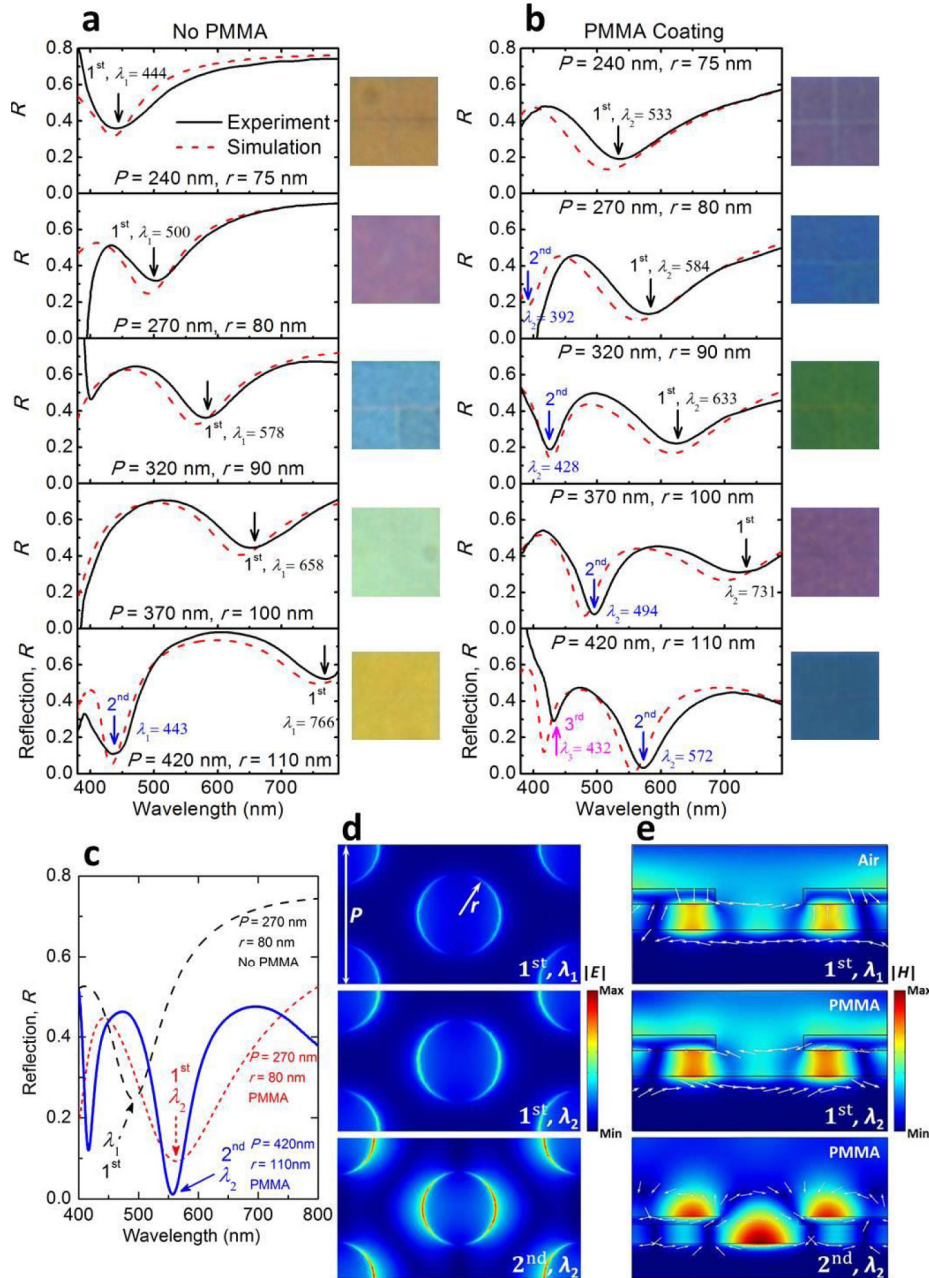


Fig. 2. Experimental (black solid) and simulated (red dashed) optical reflection spectra of the samples with successively increasing periods and hole radii (from top to bottom: $P = 240$ – 420 nm and $r = 75$ – 110 nm) for both (a) the bare and (b) the PMMA-coated samples. Insets: The measured optical images of fabricated $20 \times 20 \mu\text{m}^2$ metamaterials. (c) Calculated reflectance spectra of two selected samples (black/red dashed: $P = 270$ nm and $r = 80$ nm without/with PMMA coating; blue solid: $P = 420$ nm and $r = 110$ nm with PMMA coating). (d) Cross section of the time-averaged electric field magnitude distributions (1 nm above the top metal surface) at the resonance wavelengths (marked by the arrows in panel (c)). (e) Cross section of the time-averaged magnetic field magnitude (color map) and electric displacement (white arrows) distributions for the metamaterials without and with PMMA coating at the resonance wavelengths.

The underlying mechanism of the improved color saturation from the PMMA-coated metamaterials can be explained by the electromagnetic field distributions at the plasmonic resonances (marked by the arrows in Fig. 2(c)). For a selected sample with $P = 270$ nm and $r = 80$ nm, the calculated time-averaged electric field distributions of the first-order plasmonic resonances at λ_1 (bare structure) and λ_2 (PMMA-coated structure) are plotted respectively in the top and middle panels of Fig. 2(d), from which the excitation of propagating surface plasmons on the top Al layer is clearly shown. The presence of the PMMA layer introduces stronger electric field concentrated at the edges of the circular holes. Meanwhile, according to the calculated magnetic field distributions (color map) and the electric displacement distributions (white arrows) at the resonance wavelengths of λ_1 shown in the top panel of Fig. 2(e), the propagating surface plasmons excited at the Al-air interface interact firstly with that excited on the top Al-SiO₂ interface and are then coupled to the bottom Al-SiO₂ interface across the dielectric spacer [32], thus forming a magnetic dipole resonance with an anti-parallel current flow at the top and bottom Al-SiO₂ interfaces [33,37]. When a PMMA layer having a similar dielectric constant as that of the silica spacer is applied on the metamaterial, the refractive indices of the media around the top Al layer are matched, forming a symmetrical configuration where only the Al-dielectric surface plasmon modes are supported (i.e., Al-PMMA/Al-SiO₂ mode) and the Al-air surface plasmon mode is eliminated. These two modes form a coupled or hybrid surface plasmon mode with enhanced electromagnetic field intensity around the top Al film due to the minimized energy difference between them, as the scenario of dielectric-encapsulated transmissive Al hole arrays [31,38]. Then, the coupling of the above hybrid surface plasmon mode of the top Al film and surface plasmon waves induced on the bottom Al-SiO₂ interface can also be enhanced, resulting in a stronger magnetic dipole resonance within the PMMA-coated MIM nanostructure (as shown in the middle panel of Fig. 2(e)) and thus enhanced light absorption. On the other hand, by putting the PMMA layer, a better impedance matching condition between the plasmonic resonant mode and the free space is satisfied, resulting in a near perfect absorption at the resonance wavelength. A slight linewidth broadening of the plasmonic resonance is also observed for the PMMA-coated structure (red dashed curve in Fig. 2(c)) due to the fact that the PMMA layer induces a weaker confinement of the electromagnetic field within the silica spacer.

In order to better illustrate the effect of PMMA layer on the resonance profiles, we also investigate numerically the electromagnetic field distributions of the second-order plasmonic resonance of the 420 nm sample ($r = 110$ nm), and compare it with the first-order mode of the 270 nm sample ($r = 80$ nm) due to the close proximity of the two resonant wavelengths (Fig. 2(c)). It is noteworthy that the second-order plasmonic resonance presents not only a much stronger electromagnetic field enhancement as compared to that of the first-order mode, but also demonstrates a tremendous field redistribution and concentration of both electric and magnetic fields, as can be seen in the bottom panel of Fig. 2(d) and 2(e). For example, unlike the first-order mode where the magnetic field is concentrated within the silica spacer just under the hole edges, much more enhanced magnetic fields are well-confined in both the silica spacer at the center of each hole and the PMMA layer above the hole edges for the second-order mode. According to the above observations, the following two advantages are drawn from the second-order plasmonic mode: on one hand, the significantly enhanced electromagnetic field of the second-order mode provides a better impedance matching to the free space, resulting in near perfect light absorption; on the other hand, the well-confined electromagnetic field helps to suppress the radiative losses, reducing the linewidth of resonance as compared to that of the first-order mode. Combining the effects of the PMMA layer induced redshift of spectrum and the formation of coupled surface plasmon mode on the top Al film (as shown for the 270 nm sample) and the inherent properties of the second-order plasmonic mode, the structural color printing platform demonstrates its flexibility and applicability in creating pure colors with high saturation or brightness.

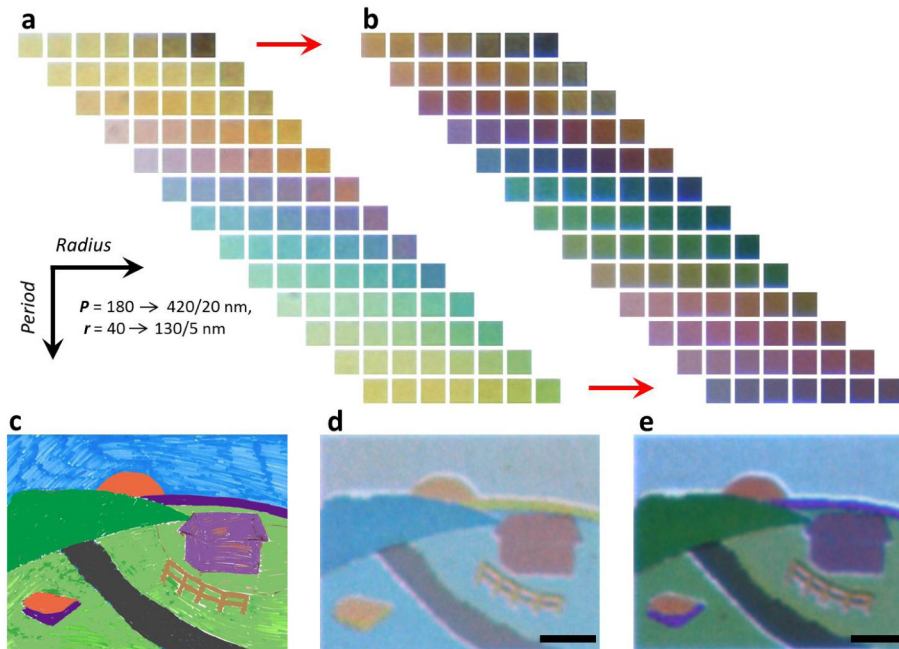


Fig. 3. (a) The measured bright-field microscope images of the bare metamaterials with period varying from 160 nm to 360 nm and hole radius ranging from 40 nm to 120 nm. (b) The bright-field microscope images of the PMMA-coated structures. (c) Original image of our created watercolor painting. (d) The measured optical microscopy image of the uncoated plasmonic painting. (e) The measured optical microscopy image of the PMMA-coated plasmonic painting. Scale bars: 10 μm .

To further illustrate the effect of the protective PMMA layer on perceived color appearances of the above plasmonic metamaterials, the bright-field microscope images of color palettes including more than 90 fabricated samples without and with the PMMA coating are compared in Fig. 3. The lattice period P ranges from 180 nm to 420 nm with a 20 nm step and the hole radius r increases from 40 nm to 120 nm with a 5 nm step. As shown in Fig. 3(b), three primary colors as well as intermediate colors are achieved with high color purity and saturation resulting from the addition of the PMMA layer. The gamut of the color palette indicates that by making the appropriate combination choice of the structure lattice period and hole radius and by taking into account the thin polymer layer, a specifically desired color appearance can always be tailored [13]. To demonstrate the applicability and suitability of the aluminum plasmonic metamaterials for color printing applications, a micrometer scale plasmonic printed copy of a watercolor art painting we drawn [Fig. 3(c)] is fabricated and the visual performance of the plasmonic painting without and with the PMMA coating is tested under microscope. By choosing the appropriate lattice periods and hole radii for each colored area and also by taking into account the effect of the frequency redshift induced by the PMMA layer, the desired image colors are well reproduced with a relative higher color brightness and visual contrast, as illustrated in the image of the PMMA-coated plasmonic painting [Fig. 3(e)] presenting a better color fidelity as compared to that obtained for the uncoated one [Fig. 3(d)].

4. Angular dependence of optical spectral responses

The angular dependence of the optical spectral response is also investigated by numerical simulation for a PMMA-coated metamaterial with $P = 270$ nm and $r = 80$ nm under both s -polarized (electric field parallel to y axis) and p -polarized (magnetic field parallel to y axis)

incidence, as shown in Fig. 4. It is noted that the excitation of surface plasmons via the lattice coupling limits the angle independence of the reflection spectra for the p -polarized light. However, the effect of lattice coupling on the spectral response is much less pronounced for the s -polarized light as shown in Fig. 4(b), where the minimum reflection remains lower than 5% even at large incident angles (70°), benefited from a strong, robust magnetic dipole resonance, although a small resonance splitting is observed at incident angles larger than 30° . The angle-resolved chromaticity coordinates under the s -polarization have been calculated from the simulated optical reflection spectra [Fig. 4(c)], which confirms a stable color appearance under large viewing angles up to 70° .

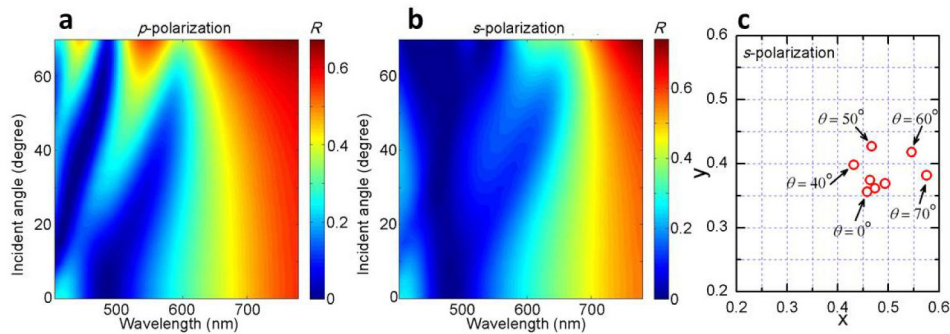


Fig. 4. (a) Incident angle dependence of the simulated reflection spectra under (a) the p -polarized light and (b) the s -polarized light for the PMMA-coated metamaterial with $P = 270$ nm and $r = 80$ nm. (c) Incident angle resolved chromaticity coordinates calculated from the reflection spectra under the s -polarized light.

5. Broadband absorptance for achieving black color

Finally, black color can also be designed and demonstrated in the PMMA-coated aluminum metamaterials by utilizing both the first-order and the second-order plasmonic resonances, where broadband near perfect light absorption covering the entire visible frequency range is simply achieved by adjusting the hole arrays of triangular lattices. Our approach to realize broadband perfect absorbers is in contrast to previous works achieved by employing relatively complicated nanostructures such as multiple resonators within one unit cell [39,40] and three-dimensional tapered multilayer structures [41]. As shown in Fig. 5(a), due to the coexistence of both the first-order and the second-order plasmonic resonances and the satisfied impedance matching condition to the free space, the optical reflection intensity across the entire visible spectrum is significantly reduced by the addition of the PMMA coating for a selected sample with $P = 340$ nm and $r = 120$ nm, which results in the near perfect light absorption at the two plasmonic resonance wavelengths at 480 nm and 610 nm of the first-order and the second-order modes, respectively. The experimental results shown in Fig. 5(b) agree with the numerical simulations and the measured absorption of over 0.8 is obtained in the wavelength range of 400–750 nm as shown in the inset. The microscope images of the sample with and without PMMA coating further verify that an almost pure black color is perceived under bright field optical microscope when a thin PMMA layer is coated on the structure.

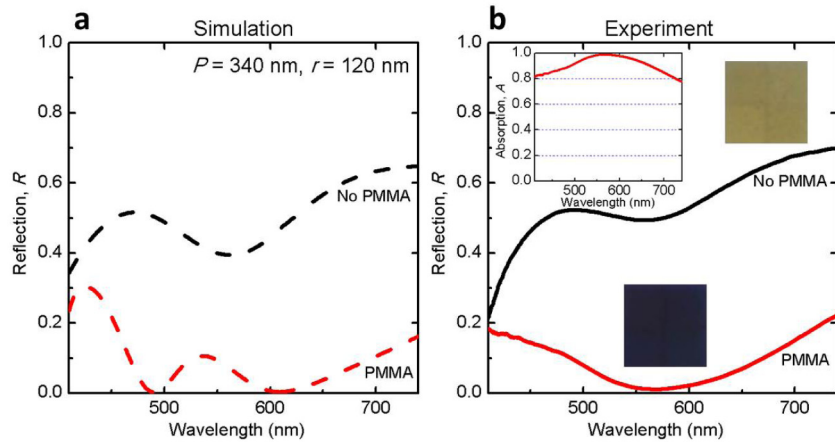


Fig. 5. (a) Calculated reflectance spectra of the designed metamaterial with $P = 340$ nm and $r = 120$ nm without (red dashed) and with (black dashed) PMMA coating for realizing pure black color. (b) Measured reflectance spectra of the fabricated metamaterial without (red solid) and with (black solid) PMMA coating. Insets: Optical reflection microscopy images of the fabricated sample and the corresponding absorption spectrum of the PMMA-coated one.

6. Conclusion

In summary, we have demonstrated a structural color generation platform presenting high spatial resolution and high color saturation. Aluminum metamaterials with tunable first-order and second-order plasmonic resonances and near perfect light absorption across the visible frequency range have been achieved by simply scaling the lattice period and hole radius in the structural design. A thin polymer coating layer induces not only a redshift in the spectra, but also a coupled surface plasmon mode of the top metal layer that helps to form a stronger magnetic resonance within the MIM structure, resulting in an enhanced light absorption. Furthermore, a second-order plasmonic resonance is induced by the polymer layer with well-confined and significantly enhanced electromagnetic fields. These two effects thus enable the resonant modes to satisfy the impedance matching condition to the free space with the reduced linewidth, leading to improved color performances such as enhanced color purity and saturation in the aluminum-based color generating metamaterials. Additionally, the polymer coated metamaterials exhibit low dependences on oblique incidence angles for the s -polarized light. We have also demonstrated the black color with the designed PMMA-coated structures. Our proposed pigment-free CMYK structural color printing platform utilizing aluminum plasmonic metamaterials are well suited for applications such as anti-counterfeit tag and security marking where erosion- and friction-resistant, robust color performance is required. Furthermore, the top and bottom metal layers of the metamaterial can be integrated as the electrodes for functional electro-optic devices.

Appendix

1. Numerical simulation

Finite element method (FEM) simulations are performed to obtain the optical reflection spectra and field distributions using COMSOL Multiphysics. In the simulations, periodic boundary conditions are employed along the x and y axes to account for the periodic arrangement of the unit cells. Perfectly matched layers (PMLs) surrounded by scattering boundary conditions are utilized along the propagation direction (perpendicular to the planar metamaterial) in order to avoid multiple reflections due to the geometry truncation. Measured permittivity of Al (imaginary part multiplied by factor of 2 to account for surface irregularities and additional losses induced by fabrication) and SiO_2 are employed in the

simulations. Besides, finite-difference time-domain (FDTD) simulations are also carried out to check the results obtained by the FEM method.

2. Metamaterial fabrication

The metal-dielectric-metal three layer stack consisting of a top 30 nm aluminum (Al) layer, a 45 nm silica (SiO₂) spacer and a bottom 100 nm thick Al mirror is deposited at room temperature on a silicon wafer by a combination of reactive magnetron sputtering and electron-beam evaporation, with a base-pressure of 2×10^{-8} Torr. Samples are transferred between physical vapor deposition systems through a load-lock at a pressure of 2×10^{-7} Torr or better. The circular holes of triangular lattices are patterned on the top of the first Al layer of the metamaterial structure using a one-step focused ion beam milling (FEI Helios Nanolab 600 DualBeam) with a gallium ion current of 28 pA and an accelerating voltage of 30KeV. Then a thin layer of PMMA (950-A2 in anisole, Michrochem), a commonly used positive electron-beam resist, is spin-coated (2,000 rounds per min) on top of the fabricated aluminum metamaterials. We choose PMMA in the present work due to its chemical and mechanical stability and the accurate control of the thickness by adjusting the spin speed or the molecule concentration. The thickness of the coated PMMA polymer layer is also determined through X-ray reflectivity (Philips X'Pert-MRD) measurement.

3. Optical spectrum characterization

We characterize the optical reflection spectra of all samples in the visible range (400–800 nm) with a home-built optical measurement system. Halogen illumination is directed to the sample area through a $\times 50$ objective lens with the numerical aperture of 0.42 and the reflected light from the metamaterial is collected by the same objective lens and collimated through a pinhole to define the sample area. Subsequently, the collected signal is directed to a fiber-coupled optical spectrometer (LR1, ASEQ instruments) to record the reflection spectra. The measured reflection spectra of all samples are then normalized by that from a silver coated mirror (THORLABS) which has optical reflection larger than 97.5% in the visible range.

Acknowledgments

The authors acknowledge the support from the University of Missouri Interdisciplinary Intercampus Research Program, the Ralph E. Powe Junior Faculty Enhancement Award, the 3M Non-Tenured Faculty Award, the National Science Foundation under grant CBET-1402743, U.S. Army Research Office Award # W911NF-15-1-0477, and the facility support from the Materials Research Center at Missouri S&T. This work was performed, in part, at the Center for Nanoscale Materials, a U.S. Department of Energy, Office of Science, Office of Basic Energy Sciences User Facility under Contract No. DE-AC02-06CH11357.